Mechanical Characteristics and Corrosion Behavior of Two New Titanium Alloys

Ionelia Voiculescu [1], Santiago Jose Brito-Garcia [2], Óscar M. González-Díaz [3] and Julia Mirza-Rosca [2,4,*]

1   Faculty of Industrial Engineering and Robotics, Politehnica University of Bucharest, 060042 Bucharest, Romania; ioneliav@yahoo.co.uk
2   Mechanical Engineering Department, University of Las Palmas de Gran Canaria, 35017 Las Palmas de Gran Canaria, Spain; santiago.brito@ulpgc.es
3   University Institute of Environmental Studies and Natural Resources (i-UNAT), University of Las Palmas de Gran Canaria, 35017 Las Palmas de Gran Canaria, Spain; oscar.gonzalez@ulpgc.es
4   Materials Engineering, and Welding Department, Transilvania University of Brasov, 500036 Brasov, Romania
*   Correspondence: julia.mirza@ulpgc.es

Abstract: While Ti6Al4V is one of the most used titanium alloys in the biomaterials field, it is not without its challenges and limitations, among which very important is the modulus mismatch with the bone. This modulus mismatch can lead to stress shielding potentially leading to bone resorption and implant loosening. Researchers continue to explore alternative materials and modifications to address this challenge and improve the performance of biomaterials. Two new fabricated titanium alloys Ti-10Al and Ti-4Fe are analyzed in this paper from corrosion and elastic modulus points of view. Metallography, microhardness, open circuit potential, DC electrochemical linear polarization, and Electrochemical Impedance Spectroscopy were performed. It was found that the corrosion resistance measurement for the Ti4Fe alloy is two orders of magnitude lower than for the Ti10Al alloy as determined by the equivalent circuit simulation, which is also supported by the similar disparity in the corrosion rate values for the two alloys which was determined using the DC method. The modulus of elasticity values were fairly close, hovering about 35GPa, and were lower than those of many commercial alloys.

Keywords: Ti10Al; Ti4Fe; metallography; corrosion; EIS

1. Introduction

The improvement of people's health and well-being is a basic goal shared by the areas of engineering and medicine, which explains their strong relationship. Medical growth and advancement depend on the application of technical and technological engineering solutions [1]. In this situation, biomaterials are utilized, and the crucial requirement of biocompatibility must be met by every biomaterial intended for medical application. The term "biocompatibility" describes a substance's capacity to perform its intended task in a medical procedure without having a negative impact on the body [2]. A number of qualities are necessary for biomaterials to be successful [3], including high ductility, fatigue resistance, wear resistance, insufficient cytotoxicity, a combination of high strength and a low Young's modulus which is equivalent to human cortical bone (which ranges from 10 to 30 GPa), and the capacity to link well with the bone around them.

Currently, a variety of materials are employed, such as metallic alloys (which are the most common), ceramics, polymers, and composites [4]. Metallic alloys used for medical devices like Ti6Al4V, NiTi alloys, CoCrMo alloys, and 316L stainless steel, make up around 70–80% of implants [5].

When metallic implants are used, corrosion is a major worry since it might cause implant failure later due to material degradation. Because of their mechanical qualities, low modulus of elasticity, and thermally stable properties, titanium and its alloys are

increasingly recognized as appropriate biomaterials for a wide range of applications [6]. The ability of titanium to form a persistent oxide film on its surface accounts for its outstanding corrosion resistance.

Several kinds of titanium-based alloys exist, such as α, α + β, and β titanium alloys. The chemical design, which must include components that stabilize specific kinds of microstructural phases, can be chosen to produce a particular type of structure [7,8]. Al, O, N, and C are the components that stabilize the Alpha phase in titanium alloys, while Fe, Mn, Cr, Cu, Ni, and Si stabilize the Beta phase. Other elements, including V, Nb, Mo, and Ta, have effects that are beta-isomorphous [9,10].

Aluminum stabilizes the alpha phase and raises the temperature required for the beta transformation in the Ti-Al system [11]. Although it is a plentiful element in nature, little is known about how aluminum works in the human body. Despite being acutely harmful only in extremely high concentrations, chronic aluminum toxicity, particularly its links to neurological issues, has received more attention of public awareness in recent years. Even if links to different diseases such as reduced skeletal mineralization, brain neurotoxicity, kidney disease, etc., there is no scientific consensus regarding this, therefore Al is still utilized in an existing biomedical alloy, Ti6Al4V [12,13].

Elements that stabilize the beta phase are necessary to decrease the titanium alloy's Young's modulus value, which is typically between 103 and 120 GPa, in order to approach the level of cortical bones for this parameter (10 to 30 GPa) [14,15]. Some titanium alloys from Ti-Mo or Ti-Mo-Zr are alloying systems, and are considered as biomaterials that also contain a fair content of Al or Fe [16].

Iron is a β-eutectoid stabilizer element in Ti-alloys. For an amount of 44 at% Al, the maximum solubility of iron in Alpha-Ti is around 1 at% Fe [17]. The toxicity of iron is quite low [18], and the products of the oxidation reactions are not retained in tissues since they are promptly metabolized [19]. Due to their excellent corrosion resistance, high wear resistance, biocompatibility, and favorable mechanical properties, for example, an inferior elastic modulus in contrast to other biocompatible metallic materials [6,20,21], binary Ti-Fe alloys are researched as potential materials for biomedical applications. A viable substance for solid-state hydrogen storage purposes is the binary intermetallic phase TiFe [22,23]. Since excess amounts, especially of Fe^{2+} ions, are toxic, this element must be kept in a solid solution or by forming stable compounds resistant to dissolution in biological fluids. But nowadays, high-purity iron is currently considered a biomaterial with good compatibility [24]. Therefore, in our research, we wanted to analyze the results that can be obtained if we add high-purity iron to a titanium matrix containing small amounts of Al or V. At the same time, we anticipated that the iron would form finely dispersed compounds that allow to increase the mechanical strength of the matrix.

In some situations, certain accessories of medical devices are needed, which are in direct contact with living tissue only for short periods of time. For such biomedical applications, in the paper two new Ti alloys containing various concentrations of Al, V, or Fe were designed and obtained by melting in VAR equipment. To evaluate the usefulness of these new alloys, the modulus of elasticity was determined, and the metallographic microstructure, corrosion resistance, and microhardness were studied.

2. Materials and Methods

2.1. Material Preparation

Table 1 displays the chemical compositions (%wt) of the investigated alloys. These alloys were created in a vacuum arc remelting furnace (VAR), model MRF ABJ 900 (Materials Research Furnaces, LLC, Allenstown, NH, USA), that used the regulated rate of fusing a consumable electrode in the vacuum created by an electric arc between an electrode and an ingot.

Table 1. Ti14Fe/Ti10Al experimental samples' chemical composition (wt %).

Sample	Ti (%)	V (%)	Fe (%)	Al (%)
Ti4Fe	93.20	0.80	4.00	2.00
Ti10Al	89.50	0.50	-	10.00

For the examined samples, many procedures were completed before performing the electrochemical, metallographic, and bending tests. The specimens were cut into tight sticks using a metallographic cutting machine Buehler IsoMet 4000 precision saw (Chicago, IL, USA). Then, the samples were embedded by adding epoxy resin into a mold, which was demolded after 24 h. Before performing the bending test, the specimens were cut again into very thin slices. The samples were then polished with an applied force of 20 N at an average speed of 300 rpm employing the Struers TegraPol-11 polished equipment (Copenhagen, Denmark).

The process of progressive carbide grinding was used. The carbide abrasive sheets with progressively finer grits from 800 grit to 2500 grit were used. Finally, an alumina suspension of 0.1 μm was applied to polishing cloths. These methods of sample preparation for metallographic analysis were compliant with ASTM E3-11 (2017) [25]. For mechanical studies, very thin slices around 1.5 mm wide were again cut vertically on the cutting machine.

2.2. Microstructure

The different states and compounds that make up a metallic substance and any contamination or potential mechanical faults are arranged spatially in metallography. Each sample was immersed in a solution of 100 mL water, 3 mL hydrofluoric acid, and 6 mL nitric acid for approximately 25 s. For optical examinations of the etched surface, the OLYMPUS PME 3 microscope (Olympus Corp., Tokyo, Japan) was employed. FE-SEM Zeiss Sigma 300 VP scanning electron microscope (Carl Zeiss, Jena, Germany) was used coupled with an energy-dispersive X-ray spectrometer (EDS) for elemental analysis. A D8 ADVANCE XRD diffractometer (Bruker™, Karlsruhe, Germany) was employed to perform the phase analysis of the samples. For the purpose of the study, a CuK radiation (1.5406 Å) with a step size of 0.02°, a power of 45 kV, and a current of 40 mA, in the range of 2θ = 20–100 was employed.

2.3. Electrochemical Tests

For the electrochemical test, the sample (from a now working electrode) is inserted in a system with other two electrodes—a saturated calomel electrode for the reference electrode and a platinum electrode for the counter electrode. The area of all the samples was picked so that the studies could be done. The Ringer solution from Grifols Laboratories (Barcelona, Spain) had the following mmoles per liter concentrations: Na^+ 129, Cl^- 111, Lact—27, K^+ 5.4, and Ca^{2+} 1.8.

Corrosion potential, then linear polarization, and electrochemical impedance spectroscopy were carried out with the BioLogic Essential SP-150 potentiostat from Seyssinet-Pariset in France.

Initially, the samples were submerged in the Ringer solution for 24 h to record the open-circuit potential. To ensure that the experiments could be reasonably reproduced, they were run three times.

For corrosion rate, the experiments were conducted using the "Linear Polarization" technique [26], and its viability was assessed by providing the specimen's surface area and the test period of 20 min. In this instance, the polarization resistance was estimated using the potential range of 25 mV against E_{corr} and a sweep rate of 0.166 mV/s. [27]. The corrosion rate estimations for each sample were obtained using EC-Lab's "Tafel Fit" method after linear polarization curves were performed.

"Potentio Electrochemical Impedance Spectroscopy" was chosen for the impedance measurement and the surface value and frequency range were provided. This measurement

was repeated three times for each sample and Nyquist and Bode diagrams were used to display the experimental data [28].

2.4. Three-Point Bending Test

The Bose ElectroForce® 3100 equipment (Framingham, MA, USA), which meets the ISO 7438:2020 [29] and has a maximum load of 20 N, was used to perform the three-point bending technique.

According to the length of the specimen, every rectangular cross-section piece was positioned in the testing equipment, with the spacing between supports ranging from 12.55 to 27.37 mm. During the experiment, the sample being studied was loaded vertically and bent until it reached its yield stress or cracked at a linear velocity of 3 mm/s at its center. The collected data of the force that was used against the displacement of the specimen were plotted to measure the modulus of elasticity and the slope was calculated.

2.5. Microhardness Test

Twelve measurements for each sample were made using the Future Tech FM-810 hardness tester (Kawasaki, Japan) for the applied loads of 1, 5, and 10 g, according to ISO 14577-1:2015 [30]. As the stress increases, the mark may comprise parts of many phases, giving a rough estimate of the material's overall hardness. It is likely that the mark will only be found when very light weights are applied, allowing the hardness of that phase to be determined. The iVicky program was used to measure the diagonal lengths and to compute the Vickers microhardness values automatically. Plotting was done between the number of indents produced and the hardness.

3. Results

3.1. Metallography

Metallography is widely used in various industries, including metallurgy, materials science, manufacturing, and engineering. It helps to understand the structure-property relationships of materials and ensure the quality and performance of metal components in different applications. After the chemical etching, significant metallographic images of the analyzed alloys can be seen in Figure 1.
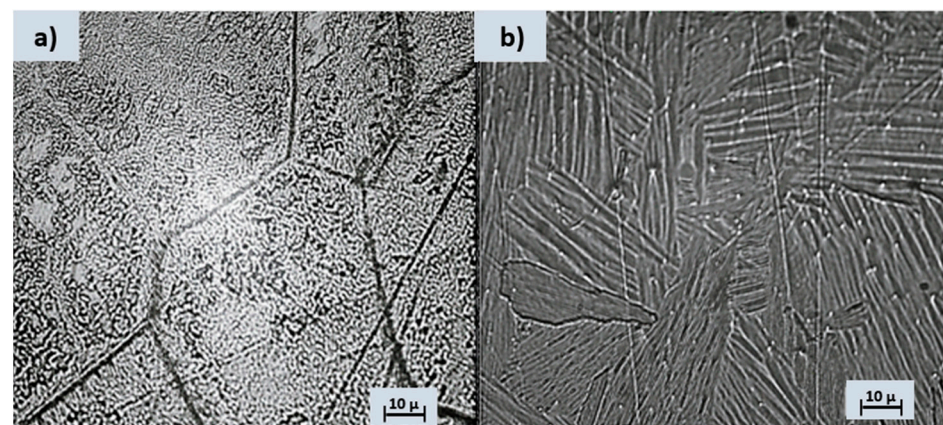
Figure 1. Optical microstructure following Kroll reagent etching for (**a**) Ti4FeE and (**b**) Ti10Al.

The Ti4Fe alloy reacted easily with the chemical attack solution so that its microstructure can be clearly seen, with the distinct highlighting of the grain boundaries. Two distinct phases can be easily identified, namely the β-Ti phase (dark area of the image) and TiFe (bright area of the image) [31], see Figure 1a. In the case of the Ti10Al sample, aluminum is an α-stabilizer of titanium, so the structure obtained for this alloy is a Widmanstätten-like structure [32]: the α-sheet colonies are thick and parallel (Figure 1b). The Al-rich titanium alloy contains equiaxial grains of alpha-solid solution. Some gamma precipitates appear

to have nucleated on the grain boundaries and grown into the striated alpha grains. The computation of the calculated crystalline phase in the XRD spectra (Figure 2d) yields 77.5% for Ti4Fe and 76.4% for Ti10Al. As can be seen from the EDS diagram (Figure 2c), both alloys contain different concentrations of Al and small amounts of V, and the Ti4Fe alloy additionally contains Fe.
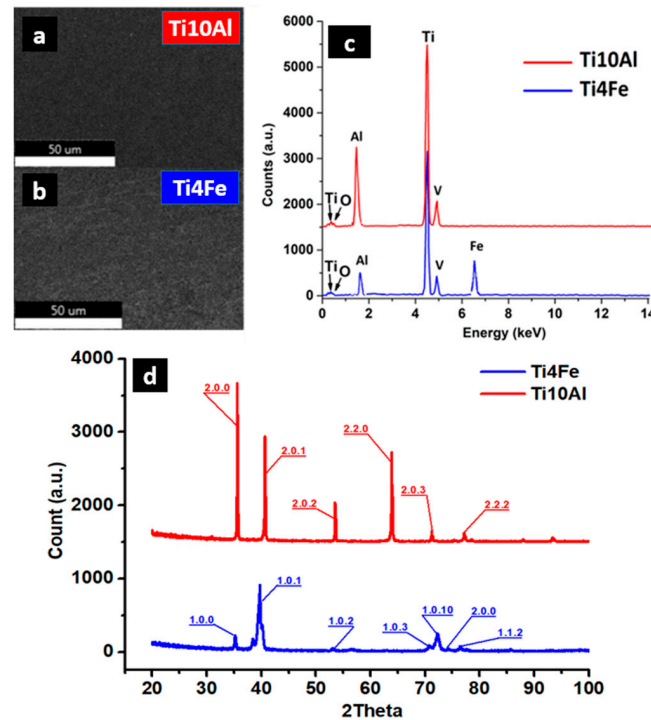
Figure 2. SEM images (**a**,**b**) of the samples with corresponding EDS spectra (**c**) and XRD spectra (**d**).

Although the samples were melted under the protective atmosphere of argon, small amounts of oxygen are present in both alloys. Depending on the concentration of the other alloying elements, oxygen can increase the mechanical resistance in titanium alloys, with acceptable ductility values. Interstitial solid solutions and complex oxides can also cause increased corrosion resistance. In the sintered Ti-6Al-4V alloy, the critical oxygen content is about 0.33 wt%, while in additive manufacturing alloy, the critical range can be between 0.22 to 0.4 wt% [31]. The experimental alloys analyzed in the paper were produced in a vacuum remelting plant, which allowed obtaining low oxygen concentrations, between 0.13 and 0.2 wt%.

3.2. Electrochemical Tests

3.2.1. Corrosion Potential (E_{corr})

When a metal is placed in an electrolyte, a redox reaction takes place at the metal's surface, causing the release or absorption of electrons. This process creates a potential difference between the metal and the surrounding solution. The open circuit potential is a measure of this voltage difference. Corrosion potential development over time is a quantitative indicator of corrosion behavior, albeit there is yet insufficient data to conduct a comprehensive analysis.

Figure 3 displays the corrosion potential versus time curves after 1 day of immersion in Ringer's solution of the studied alloys. Table 2 shows the corresponding initial potential values, after 6 h and 24 h immersion of the samples. The potential of Ti10Al fluctuates and increases indicating the passivation of the sample during the exposure. The potential of Ti4Fe decreases with almost 300 mV during the immersion time, suggesting the sample is susceptible to corrosion and a corrosion product layer is formed on the surface which is not thermodynamically stable in these conditions.
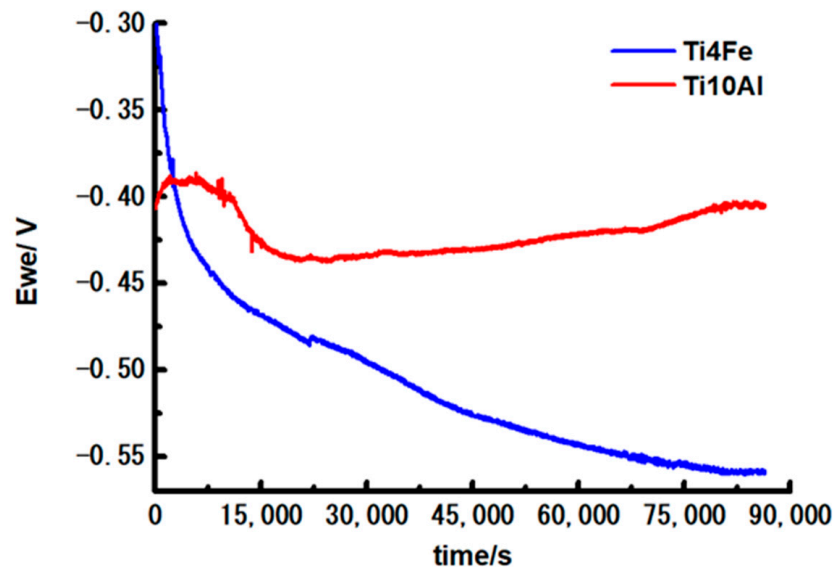
Figure 3. Curves of corrosion potential of Ti10Al and Ti4Fe materials during a 24-h immersion.

Table 2. OCP values of the two samples: initially, after 6 h and a day of immersion in Ringer Grifols solution.

Sample	OCP (V) vs. SCE		
	Initial	After 6 h	After 1 Day
Ti4Fe	−0.277	−0.484	−0.558
Ti10Al	−0.407	−0.434	−0.397

3.2.2. Corrosion Rate (CR)

Figure 4 displays the outcomes of the linearly polarized approach using a semi-logarithmic scale of the data.
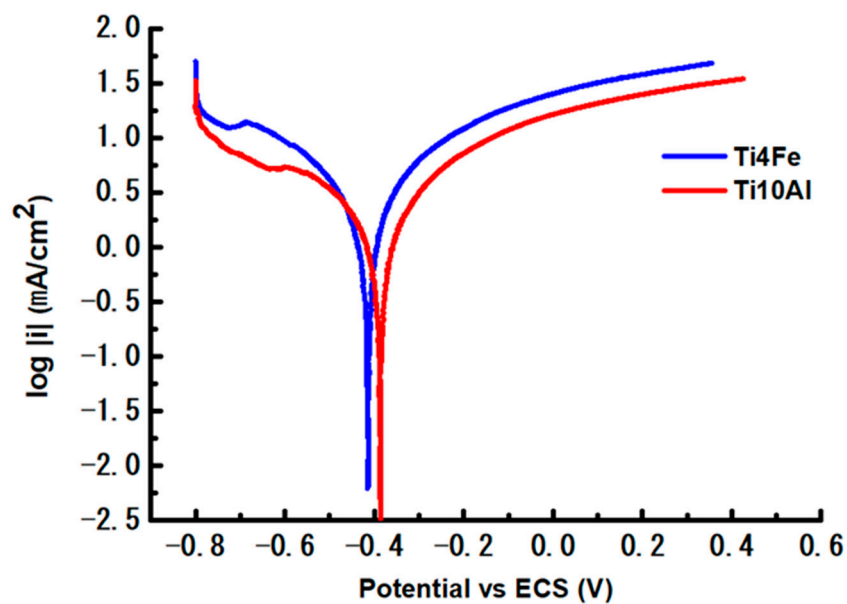

Figure 4. Polarization curves of the two test samples.

According to Table 3, Ti4Fe displays higher values of E_{corr} and I_{corr} than Ti10Al, which indicates the extent to which the alloy has been oxidized. The curves shown log i versus

potential in the range $E_{corr} \pm 0.25$ V were used to get the Tafel slopes (Figure 4). A corrosion-prone alloy is going to have β_a smaller than β_c, while a passivation-prone alloy should have a β_a bigger than β_c. The Ti10Al material in our case has a predisposition to passivate and it allows a passive coating to develop on its surface. Table 3 also includes the Tafel curve slopes, corrosion rate (CR), equivalent weight (EW), density (d, g/cm^3), and area (A, cm^2) of each sample. The corrosion rate is calculated with the corrosion current (I_{corr}, Amp), constant (K), and corrosion rate parts (3.272 mm/A-cm-year).

$$CR = \frac{I_{corr} \cdot K \cdot EW}{d \cdot A} \tag{1}$$

Table 3. Corrosion values for all the samples that were evaluated.

Parameters	Ti4Fe	Ti10Al
E_{corr} (mV vs. Ref)	−418.03	−385.33
I_{corr} (µA/cm^2)	2.40	1.68
β_c (mV/dec)	301.70	377.00
β_a (mV/dec)	292.60	447.26
Equivalent weight (g/eq)	47.80	45.80
Density (g/cm^3)	4.62	4.33
Surface (cm^2)	0.58	0.59
Corrosion rate (mm/year)	140.2×10^{-3}	98.86×10^{-3}

In this case, a minimum CR of 98.60×10^{-3} mm/y (Ti10Al) and a maximum CR of $140.20 \cdot 10^{-3}$ mm/y (Ti4Fe) were achieved.

In a physiological medium, the corrosion rate of iron is strongly influenced by the rate of the cathodic reaction and the quantity of the dissolved oxygen due to the reactions:

$$Fe \rightarrow Fe^{2+} + 2e^- \tag{2}$$

$$2H_2O + O_2 + 4e^- \rightarrow 4OH^- \tag{3}$$

From the Pourbaix diagram [32], ferrous hydroxide is the most common corrosion product due to the reaction:

$$Fe^{2+} + 2OH^- \rightarrow Fe(OH)_2 \tag{4}$$

The coordination complex of iron oxides is another typical result of Fe corrosion at physiological pH ($FeO \cdot Fe_2O_3$). Different substances resulting from iron dissolution, such as iron carbonates, iron chloride, iron phosphates, and iron sulphates were identified since the human body environment is rich in salts, carbonates, phosphates, etc. [33]. Because it is essential for so many key metabolic processes such as oxygen detection, transport, short-term oxygen preservation, catalysis, movement of electrons, and energy production, iron is essential for life. The protein ferritin offers secure storage for the iron part kept by the cell, whereas most of the absorbed iron will end up in the plasma. Red blood cells mature and are expelled through the digestive tract together with any leftover iron that was previously retained. This manner of iron release and bodily iron loss is significant [33]. Other ways that iron is released include bleeding, sweating, and expulsion through the skin. These different mechanisms are crucial since the human liver and renal excretion of iron are unregulated processes. The body can, however, self-regulate when its ideal iron levels are surpassed, for instance by reducing the amount of iron it takes in from food [34]. Given the previously described process of iron metabolization in the body, we can assume that the presence of Fe does not negatively impact the organs and proper functioning of the human body.

3.2.3. Electrochemical Impedance Spectroscopy (EIS)

Electrochemical impedance spectroscopy is a high-throughput technique for investigating the interfacial properties associated with chemical reactions occurring on alloy surfaces. Since EIS is a stable state method and can probe this scenario from 100 mHz to 100 KHz and can quantify incredibly small signals, it has a lot of advantages over other electrochemical techniques.

The EIS experimental data are shown in the Nyquist graph (Figure 5) and Bode graphs (Figures 6 and 7).

A plot of the imaginary part of the impedance (Y-axis) against the real part of the impedance (X-axis), see Figure 5, has an incomplete semicircular shape for both samples. It can be observed that the capacitive loop has a higher diameter for Ti10Al than for Ti4Fe which indicates a low polarization resistance for Ti4Fe or what is the same, a low resistance to corrosion [35].
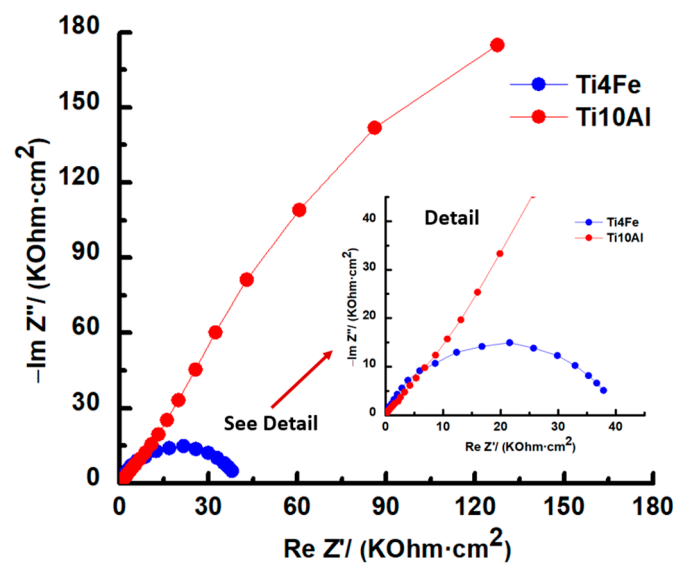
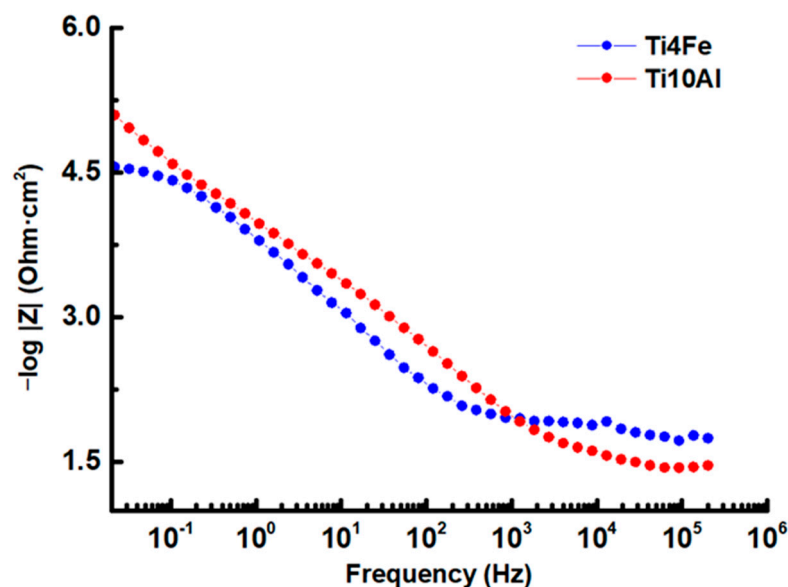**Figure 5.** Nyquist diagrams for Ti4Fe and Ti10Al in Ringer's solution.

Figure 6. Bode-IZI impedance diagram for Ti4Fe and Ti10Al in Ringer's solution.
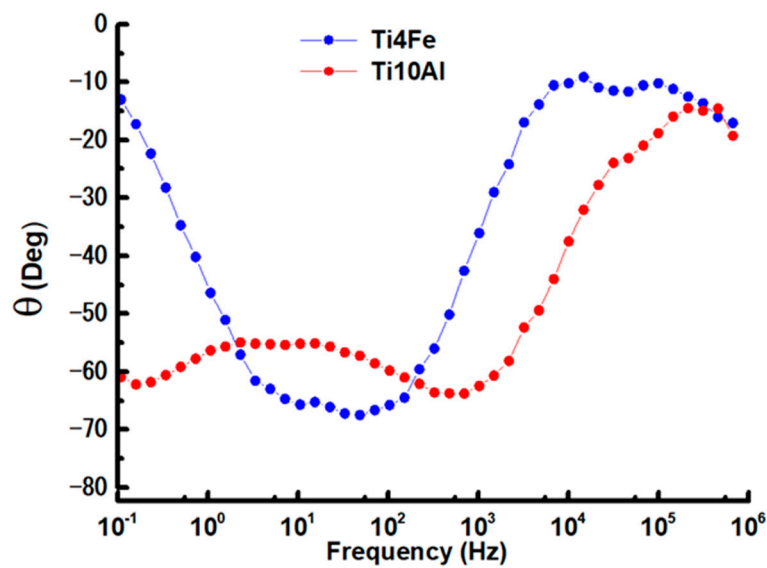
Figure 7. Bode phase graphs for Ti4Fe and Ti10Al in Ringer's solution.

Bode plots were used to show the logarithmic frequency dependence of the impedance modulus and phase shift angles of the specimens of Ti4Fe and Ti10Al dissolved in Ringer's solution. The Bode impedance and phase diagrams are shown in Figures 6 and 7, respectively, and the results at E_{corr} are shown in Table 4.

Table 4. Results from the Bode diagrams of the samples being studied at E_{corr}.

Sample	Potential (V)	Maximum Z (Ω)	Maximum θ (Deg)
Ti4Fe	−0.517	37,901.75	70.01
Ti10Al	0.010	127,471.95	63.78

When the frequency is as low as 0.1 Hz, in the Bode-IZI diagram (see Figure 6) for Ti10Al, a significant shift of the impedance module in favor of higher values is seen, emphasizing a rise in corrosion resistance brought on by the development of the passive layer on the sample's surface.

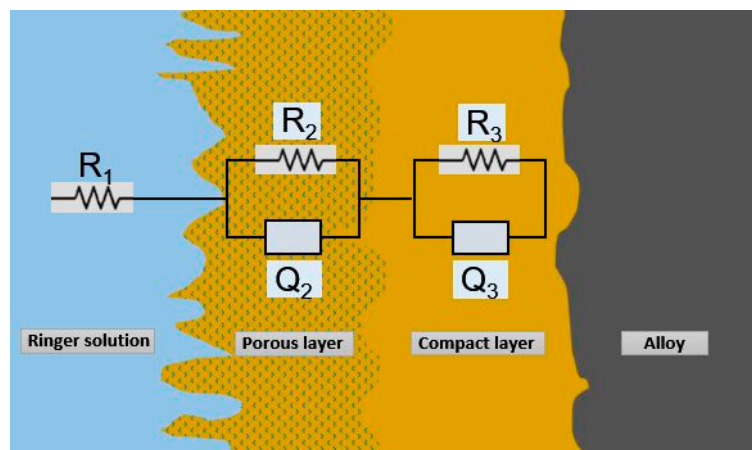The samples' phase angle curves and the highest values are shown in Figure 8 and Table 4.

Figure 8. Equivalent circuit R(QR)(QR).

The equivalent circuit design R(QR)(QR), which best matches the experimental impedance values for the alloys Ti4Fe and Ti10Al in the study, is shown in Figure 8.

According to the model and Equation (1), R_1 represents the resistance of the electrolyte, R_2 and R_3 represent the resistances of the porous and compacted passive films, respectively, and Q_2 and Q_3 represent the capacitances of the passive films.

The semi-infinite Warburg impedance (n = 0.5), the resistor (n = 0.0), and the capacitor (n = 1.0) are all accurately reproduced by the constant phase element as functions of the values of the parameters n_2 and n_3, and the applied frequency, f.

$$Z(f) = R_1 + \frac{R_2}{R_2 \cdot Q_2 \cdot (j \cdot 2 \cdot \pi \cdot f)^{n_2} + 1} + \frac{R_3}{R_3 \cdot Q_3 \cdot (j \cdot 2 \cdot \pi \cdot f)^{n_3} + 1} \tag{5}$$

Table 5 shows that the replacement of iron with aluminum improves the corrosion resistance of the analyzed alloys.

Table 5. R(QR)(QR) circuit equivalent parameters for Ti4Fe and Ti10Al.

Parameters	Sample	
	Ti4Fe	**Ti10Al**
R_1 (ohm·cm^2)	16.74	15.73
Y_2 (S·sec^n/cm^2)	1.38×10^{-5}	3.56×10^{-5}
n_2	0.58	0.94
R_2 (ohm·cm^2)	30.85	691.60
Y_3 (S·sec^n/cm^2)	5.42×10^{-5}	5.54×10^{-5}
n_3	0.81	0.68
R_3 (ohm·cm^2)	2.27×10^4	9.80×10^6
χ^2	3.78×10^{-3}	7.01×10^{-3}

For the excellent fitting of the EIS data, a Chi-square (χ^2) value of 10^{-3} has been favored.

3.3. Three-Point Bending Test

Equation (3) was used to calculate the median values of the two specimens' elastic modulus (E), incorporating into consideration the applied load (F), the spacing of supports where the lower shank of the apparatus is placed to hold specimens (L), the moment of inertia (I), and the amount of deformation (δ):

$$E = \frac{F \cdot L^3}{48 \cdot \delta \cdot I} \cdot 10^{-3} \tag{6}$$

Because the samples have a rectangular cross-section, the moment of inertia is determined by Equation (7) in which w represents the specimen's width and h is the thickness of the specimen.

$$I = \frac{w \cdot h^3}{12} \tag{7}$$

After determining the average elasticity modulus values for each specimen, it was possible to see that the Ti10Al sample had the lowest E value (41.31 ± 6.89 GPa), while the Ti4Fe sample had the highest E value (44.46 ± 5.56 GPa). This shows that the sample with aluminum has a lower Young's modulus and is getting close to the E of human bone (7–30 GPa), Table 6.

Table 6. The alloys under study's Young's modulus.

Alloy	Sample	F/d (N/mm)	L (mm)	Length (mm)	Width (mm)	Thickness (mm)	E (GPa)
	1	19.88	9.10	22.53	0.92	0.45	44.67
	2	68.10	9.10	20.28	0.83	0.68	49.16
	3	83.55	9.10	22.47	0.98	0.76	36.59
Ti4Fe	4	11.05	9.10	22.42	0.80	0.38	47.41
	Average						44.46
	Deviation						5.56
	1	14.94	9.10	27.30	0.66	0.49	36.25
	2	2.26	9.10	27.33	0.41	0.31	34.83
	3	5.45	9.10	27.30	0.45	0.37	45.06
Ti10Al	4	9.44	9.10	12.55	0.66	0.38	49.11
	Average						41.31
	Deviation						6.89

However, for both samples, the results are lower than those for the TiMoZrTa alloy (52–69 GPa) and similar to those for the TiMoSi alloy (20–43 GPa), falling into limits that are close to those found in previous analyses.
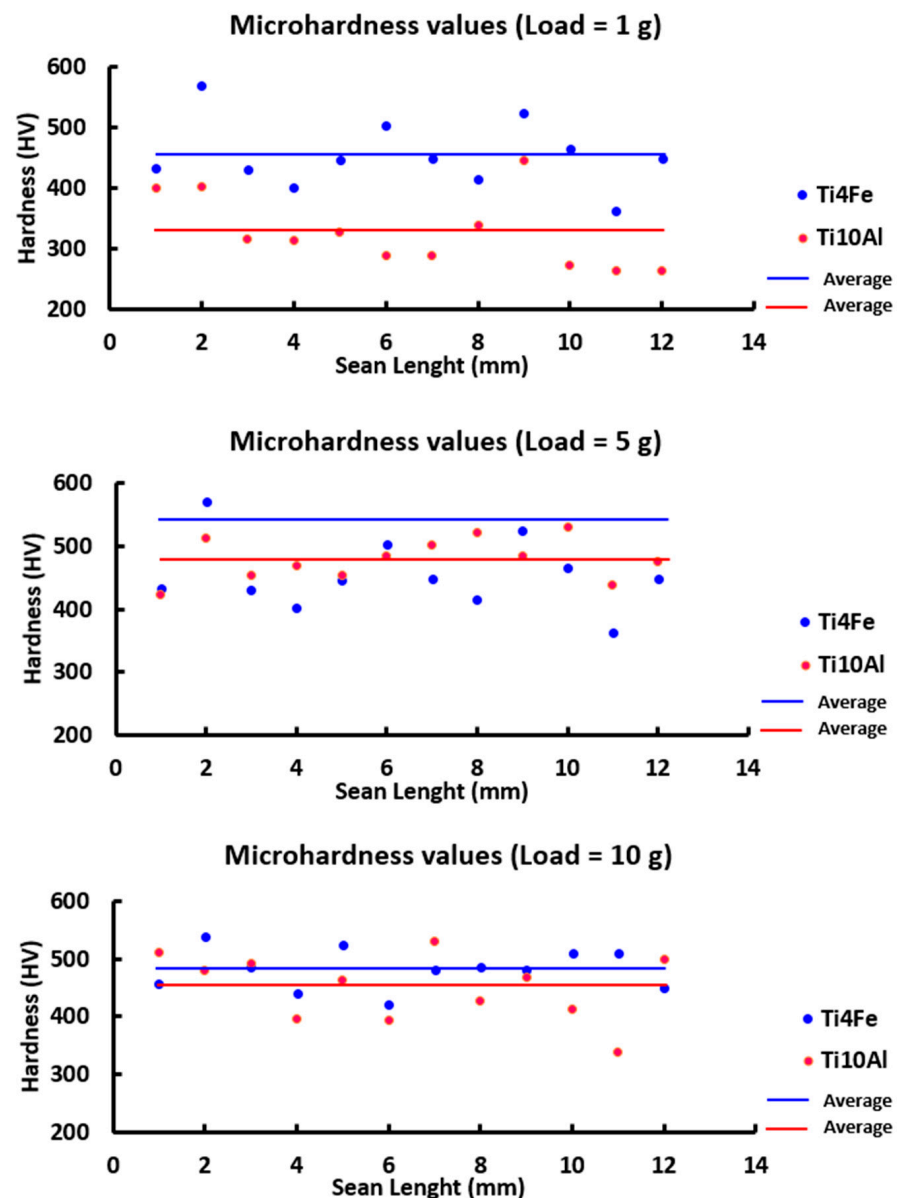
3.4. Microhardness Test

The microhardness measurements for each sample's 12 indentations are shown in Figure 9 and Table 7 along with the standard deviation, lowest and highest values, and the microhardness values in HV 0.001, HV 0.01, and HV 0.025.

Figure 9 compares the averages of the 12 indentations made on the two specimens for every load that was applied. Due to the different hardness evaluations of the alpha and beta phases and the position of the substance's crystals, some extremely high peaks can be observed in contrast to other very low ones, indicating that there are harder or softer regions on the surface of the specimens and therefore, some degree of homogeneity throughout the production of the samples. Nevertheless, the results obtained tend to be among 250 and 450 HV for each of the loads being applied.

Table 7. The four samples' microhardness values for applied stresses of 1, 5, and 10 g.

	Microhardness Ti4Fe (HV)			Microhardness Ti10Al (HV)		
Essay	1 g	5 g	10 g	1 g	5 g	10 g
1	433.00	541.00	458.00	401.00	423.00	511.00
2	570.00	512.00	539.00	402.00	512.00	480.00
3	431.00	530.00	486.00	317.00	453.00	492.00
4	402.00	511.00	441.00	315.00	468.00	397.00
5	447.00	445.00	524.00	328.00	453.00	463.00
6	503.00	551.00	421.00	289.00	484.00	393.00
7	449.00	572.00	480.00	289.00	502.00	531.00
8	416.00	582.00	486.00	338.00	521.00	426.00
9	525.00	560.00	480.00	447.00	485.00	469.00
10	466.00	618.00	511.00	272.00	531.00	412.00
11	362.00	511.00	511.00	264.00	438.00	338.00
12	449.00	569.00	449.00	264.00	476.00	498.00
Average	454.42	541.82	482.17	327.17	478.83	450.83
Deviation	56.18	44.50	34.05	60.09	33.64	57.52
Maximum	570.00	618.00	539.00	447.00	531.00	531.00
Minimum	362	445	421	264	423	338

Figure 9. For each indentation on the four materials under investigation, the microhardness values at 1, 5, and 10 g of loading.

The averages are seen more clearly in Table 7, where the Ti4Fe sample received a higher value (454.42 ± 56.18 HV) for 1g applied as well as for 5 and 10 g.

The minimum values for the 5 g load, however, were 423 and 445 HV (Ti10Al and Ti4Fe, respectively). The Ti10Al and Ti4Fe samples, respectively, attained a maximum of 531 HV and 618 HV for the 10 gf loading. Therefore, a rise in the hardness values is observed when iron is added to the samples in place of aluminum.

Additionally, the values discovered in this study are greater than those of cpTi [36], but lower than those of typical alloys such as CoCrMo (150–600 HV) and Ti6Al4V (540 HV) [37].

4. Conclusions

The research in this article analyzed and contrasted the mechanical characteristics and corrosion behavior of two titanium alloys, one with aluminum, Ti10Al, and the other with iron, Ti4Fe. By means of metallography, electrochemical tests in DC and AC current, three-point bending test, and microhardness test, several conclusions have been generated:

- The metallographic test shows an alpha structure for the Ti10Al alloy and a biphasic structure for Ti10Fe.
- The potential of Ti10Al increased during the 24 h of immersion time proving that the surface's passive coating is thermodynamically resilient under these circumstances. The open circuit potential of Ti4Fe is decreasing in time due to the corrosion process which takes place on the surface of the alloy.
- The AC corrosion resistance measurement (R_3) for the Ti4Fe alloy is two orders of magnitude lower than for the Ti10Al alloy as determined by the equivalent circuit simulation, which is also supported by the similar disparity in the corrosion rate values for the two alloys which were determined using the DC method.
- The modulus of elasticity values were fairly close, hovering about 35 GPa, and compared to several commercial alloys, they were lower.
- According to our results, the new alloy Ti10Al demonstrated good mechanical qualities (hardness and elastic modulus) and great corrosion resistance in contrast to commercial alloys.

Author Contributions: I.V. conceptualization, investigation, and management; S.J.B.-G. methodology, investigation, and data curation; Ó.M.G.-D. investigation and data curation; J.M.-R. investigation, writing—review, and editing. All authors have read and agreed to the published version of the manuscript.

Data Availability Statement: All data provided in the present manuscript are available to whom it may concern.

Conflicts of Interest: The authors declare no conflict of interest.

References

1. Bhamra, R.; Hicks, C.; Small, A.; García-Villarreal, E. Value, product delivery strategies and operational performance in the medical technology industry. *Int. J. Prod. Econ.* **2022**, *245*, 108399. [CrossRef]
2. Bandyopadhyay, A.; Mitra, I.; Goodman, S.B.; Kumar, M.; Bose, S. Improving biocompatibility for next generation of metallic implants. *Prog. Mater. Sci.* **2023**, *133*, 101053. [CrossRef] [PubMed]
3. Biswal, T.; BadJena, S.K.; Pradhan, D. Sustainable biomaterials and their applications: A short review. *Mater. Today Proc.* **2020**, *30*, 274–282. [CrossRef]
4. Simorgh, S.; Alasvand, N.; Khodadadi, M.; Ghobadi, F.; Malekzadeh Kebria, M.; Brouki Milan, P.; Kargozar, S.; Baino, F.; Mobasheri, A.; Mozafari, M. Additive manufacturing of bioactive glass biomaterials. *Methods* **2022**, *208*, 75–91. [CrossRef]
5. Niinomi, M.; Nakai, M.; Hieda, J. Development of new metallic alloys for biomedical applications. *Acta Biomater.* **2012**, *8*, 3888–3903. [CrossRef] [PubMed]
6. Zhang, L.C.; Chen, L.Y. A Review on Biomedical Titanium Alloys: Recent Progress and Prospect. *Adv. Eng. Mater.* **2019**, *21*, 1801215. [CrossRef]
7. Popa, M.V.; Vasilescu, E.; Drob, P.; Anghel, M.; Vasilescu, C.; Mirza-Rosca, I.; Lopez, A.S. Anodic passivity of some titanium base alloys in aggressive environments. *Mater. Corros.* **2002**, *53*, 51–55. [CrossRef]
8. Vasilescu, E.; Drob, P.; Popa, M.V.; Anghel, M.; Santana Lopez, A.; Mirza-Rosca, I. Characterisation of anodic oxide films formed on titanium and two ternary titanium alloys in hydrochloric acid solutions. *Werkst. Und Korros.* **2000**, *51*, 413–417. [CrossRef]
9. Kaur, M.; Singh, K. Review on titanium and titanium based alloys as biomaterials for orthopaedic applications. *Mater. Sci. Eng. C* **2019**, *102*, 844–862. [CrossRef] [PubMed]
10. Guerra-Yánez, H.; Florido-Suárez, N.R.; Voiculescu, I.; Mirza-Rosca, J.C. Corrosion behavior of new titanium alloys for medical applications. *Mater. Today Proc.* **2023**, *72*, 533–537. [CrossRef]
11. Wang, H.; Chao, Q.; Chen, H.S.; Chen, Z.B.; Primig, S.; Xu, W.; Ringer, S.P.; Liao, X.Z. Formation of a transition V-rich structure during the α' to α + β phase transformation process in additively manufactured Ti-6Al-4 V. *Acta Mater.* **2022**, *235*, 118104. [CrossRef]
12. Madeira, S.; Buciumeanu, M.; Nobre, D.; Carvalho, O.; Silva, F.S. Development of a novel hybrid Ti6Al4V–ZrO2 surface with high wear resistance by laser and hot pressing techniques for dental implants. *J. Mech. Behav. Biomed. Mater.* **2022**, *136*, 105508. [CrossRef]

13. Rana, M.; Karmakar, S.; Bandyopadhyay, A.; Roychowdhury, A. Design and manufacturing of patient-specific Ti6Al4V implants with inhomogeneous porosity. *J. Mech. Behav. Biomed. Mater.* **2023**, *143*, 105925. [CrossRef] [PubMed]
14. Eldabah, N.M.; Shoukry, A.; Khair-Eldeen, W.; Kobayashi, S.; Gepreel, M.A.H. Design and characterization of low Young's modulus Ti-Zr-Nb-based medium entropy alloys assisted by extreme learning machine for biomedical applications. *J. Alloys Compd.* **2023**, *968*, 171755. [CrossRef]
15. Walunj, G.; Desai, J.; Bohara, S.; Contieri, R.; Kothapalli, C.; Ivanov, E.; Borkar, T. Light weight- low modulus biocompatible titanium alloys processed via spark plasma sintering. *J. Alloy. Metall. Syst.* **2023**, *3*, 100018. [CrossRef]
16. Niinomi, M. Recent research and development in metallic materials for biomedical, dental and healthcare products applications. *Mater. Sci. Forum* **2007**, *539–543 Pt 1*, 193–200. [CrossRef]
17. Rosca, J.C.M.; Vasilescu, E.; Drob, P.; Vasilescu, C.; Drob, S.I. Corrosion behaviour in physiological fluids of surface films formed on titanium alloys. *Mater. Corros.* **2012**, *63*, 527–533. [CrossRef]
18. Li, Y.; Pavanram, P.; Bühring, J.; Rütten, S.; Schröder, K.U.; Zhou, J.; Pufe, T.; Wang, L.N.; Zadpoor, A.A.; Jahr, H. Physiomimetic biocompatibility evaluation of directly printed degradable porous iron implants using various cell types. *Acta Biomater.* **2023**, *169*, 589–604. [CrossRef] [PubMed]
19. Hildebrand, H.F.; Hornez, J.C. Biological response and biocompatibility. *Met. Biomater.* **1998**, 265–290.
20. Ehtemam-Haghighi, S.; Prashanth, K.G.; Attar, H.; Chaubey, A.K.; Cao, G.H.; Zhang, L.C. Evaluation of mechanical and wear properties of TixNb7Fe alloys designed for biomedical applications. *Mater. Des.* **2016**, *111*, 592–599. [CrossRef]
21. Abdelrhman, Y.; Gepreel, M.A.H.; Kobayashi, S.; Okano, S.; Okamoto, T. Biocompatibility of new low-cost ($\alpha+\beta$)-type Ti-Mo-Fe alloys for long-term implantation. *Mater. Sci. Eng. C* **2019**, *99*, 552–562. [CrossRef]
22. Sandrock, G. A panoramic overview of hydrogen storage alloys from a gas reaction point of view. *J. Alloys Compd.* **1999**, *293–295*, 877–888. [CrossRef]
23. Sujan, G.K.; Pan, Z.; Li, H.; Liang, D.; Alam, N. An overview on TiFe intermetallic for solid-state hydrogen storage: Microstructure, hydrogenation and fabrication processes. *Crit. Rev. Solid State Mater. Sci.* **2020**, *45*, 410–427. [CrossRef]
24. Khan, L.; Sato, K.; Okuyama, S.; Kobayashi, T.; Ohashi, K.; Hirasaka, K.; Nikawa, T.; Takada, K.; Higashitani, A.; Abiko, K. Ultra-high-purity iron is a novel and very compatible biomaterial. *J. Mech. Behav. Biomed. Mater.* **2020**, *106*, 103744. [CrossRef]
25. *ASTM E3-11(2017)*; Standard Guide for Preparation of Metallographic Specimens. ASTM International: West Conshohocken, PA, USA, 2017.
26. *ASTM G5-94(2004)*; Standard Reference Test Method for Making Potentiostatic and Potentiodynamic Anodic. ASTM International: West Conshohocken, PA, USA, 2004; pp. 1–12.
27. *ASTM G102-89(1999)*; Standard practice for calculation of corrosion rates and related information from electrochemical measurements. ASTM International: West Conshohocken, PA, USA, 1999; pp. 1–7.
28. *ISO 16773-1-4:2016*; Electrochemical Impedance Spectroscopy (EIS) on Coated and Uncoated Metallic Specimens. ISO: Geneva, Switzerland, 2016.
29. *ISO 7438:2020*; Metallic Materials—Bend Test. ISO: Geneva, Switzerland, 2020.
30. *ISO 14577-1:2015*; Metallic Materials—Instrumented Indentation Test for Hardness and Materials Parameters—Part 1: Test Method. ISO: Geneva, Switzerland, 2015.
31. Yan, M.; Xu, W.; Dargusch, M.S.; Tang, H.P.; Brandt, M.; Qian, M. Review of effect of oxygen on room temperature ductility of titanium and titanium alloys. *Powder Metall.* **2014**, *57*, 251–257. [CrossRef]
32. Pourbaix, M.; Zhang, H.; Pourbaix, A. Presentation of an Atlas of chemical and electrochemical equilibria in the presence of a gaseous phase. *Mater. Sci. Forum* **1997**, *251–254*, 143–148. [CrossRef]
33. Gąsior, G.; Szczepański, J.; Radtke, A. Biodegradable Iron-Based Materials—What Was Done and What More Can Be Done? *Materials* **2021**, *14*, 3381. [CrossRef]
34. Muckenthaler, M.U.; Rivella, S.; Hentze, M.W.; Galy, B. A Red Carpet for Iron Metabolism. *Cell* **2017**, *168*, 344–361. [CrossRef]
35. Socorro-Perdomo, P.P.; Florido-Suárez, N.R.; Voiculescu, I.; Mirza-Rosca, J.C. Comparative eis study of alxcocrfeni alloys in ringer's solution for medical instruments. *Metals* **2021**, *11*, 928. [CrossRef]
36. da Rocha, S.S.; Adabo, G.L.; Henriques, G.E.P.; Nóbilo, M.A. de A. Vickers hardness of cast commercially pure titanium and Ti-6Al-4V alloy submitted to heat treatments. *Braz. Dent. J.* **2006**, *17*, 126–129. [CrossRef]
37. Sandu, A.V.; Baltatu, M.S.; Nabialek, M.; Savin, A.; Vizureanu, P. Characterization and Mechanical Proprieties of New TiMo Alloys Used for Medical Applications. *Materials* **2019**, *12*, 2973. [CrossRef]